Arrays of dark optical traps on a toroidal surface

Jakub Bělín,[1,*] V. E. Lembessis,[2] A. Lyras,[2] O. Aldossary,[2,3] and Johannes Courtial[1,†]

[1] *School of Physics and Astronomy, College of Science and Engineering, University of Glasgow, Glasgow G12 8QQ, UK*
[2] *Department of Physics and Astronomy, College of Science, King Saud University, P.O. Box 2455, Riyadh 11451, Saudi Arabia*
[3] *The National Center for Applied Physics, KACST, P.O. Box 6086, Riyadh 11442, Saudi Arabia*

We have theoretically constructed light fields that can generate optical potentials representing rectangular arrays of dark optical traps on the surface of a torus. The arrays are not diffraction-limited, and their period can in principle be deeply sub-wavelength. We discuss the challenges anticipated in realising such potentials which will be of great interest for quantum simulations.

Keywords: Vortex lines, Dark optical traps, Fractional Quantum Hall Effect

I. INTRODUCTION

Light fields with tailored intensity landscapes have attracted considerable interest recently in conjunction with the development of laser cooling and trapping techniques for atoms. When the intensity pattern, generated by interfering light beams, provides optical trapping potentials, sufficiently cooled atoms can be loaded in the available trapping sites. The atomic trapping is enabled by the conservative potential resulting from the AC Stark shift of the energy levels of an atom, induced by the far-detuned optical fields. The spatial arrangement of the trapping sites can be varied considerably exploiting the tunability of the superimposed light beams, in terms of wavelength, polarization and amplitude. Additional flexibility is afforded when the light beams have spatially structured amplitude and phase profiles. Moreover, the trapping potential depth can be also varied spatially in a controlled manner. Periodic arrangements of the trapping sites, called Optical Lattices (OL), have attracted considerable interest in recent years [1]. The OL have found applications in the controlled transport of trapped atoms [2], in atomic interferometry, in building quantum information processing devices and in atomic clocks with considerably improved stability [3]. One of the most intriguing and challenging application of OL is the emulation of solid state phenomena [4]. Recent research has identified two major challenges for the successful application of OL to the study of intriguing solid state phenomena: (i) to overcome the constraints imposed by beam diffraction on the lattice spacing (it is generically limited to $\lambda/2$, with λ the light wavelength) that would facilitate the study of Hubbarb models [5], and (ii) to engineer optical potential and OL geometries that would allow the emulation of strong synthetic gauge fields (effective magnetic fields, in particular [6]) that are a prerequisite for the emulation of phenomena like the Fractional Quantum Hall Effect (FQHE) [7], [8]. An optical trapping potential of toroidal geometry is interesting per se, as any novel and unusual shape of a trapping potential. Moreover, it is potentially useful for the emulation of the FQHE. In particular, the toroidal symmetry conforms to the topological properties of the ground state of systems exhibiting the FQHE [9]. Additionally, an OL on the toroidal surface will facilitate the emulation of strong effective magnetic fields if coherent manipulation of the trapped atoms around closed-circuit paths on the lattice can be devised. Engineering such a lattice is challenging. To begin with, it involves two major tasks. First, a bright toroidal surface with a mesh of dark spot-like regions should be engineered. Second, the dark sites should be sufficiently deep so that atoms can be trapped. It would also be desirable that the spacing of the trapping sites is as short as possible, with the ultimate goal being to achieve sub-wavelength spacing [10].

To the best of our knowledge there have been no published works towards the realization of such an optical lattice. In this work, for the first time, we attempt a feasibility study towards the eventual experimental realization of such an optical lattice. We investigate the possibility of creating a light field with a bright toroidal surface on which a regular mesh of dark sites is superimposed.

Here we construct, theoretically, light fields that contain various rectangular arrays of optical traps on the surface of a distorted torus. The traps are blue-detuned, i.e. the intensities at the trap locations are close to zero and surrounded in all directions by significantly larger intensities. The separation between neighbouring traps can, in principle, be arbitrarily small — it is not diffraction-limited —, but decreasing the trap separation also exponentially decreases the intensity barrier separating the traps.

Our construction starts with scalar vortex torus knots: scalar fields that contain closed vortex lines in the shape of approximately regular spirals on a torus (with the topology of torus knots), shown schematically in Fig. 1(a,b). Such fields have previously been demonstrated theoretically [11] and experimentally [12–14] in the form of paraxial light fields. Here we generalise this construction to non-scalar fields, which are exact solutions of Maxwell's equations that hold even under the tight-focussing conditions required to reduce the size of

*Electronic address: j.belin.1@research.gla.ac.uk
†Electronic address: Johannes.Courtial@glasgow.ac.uk

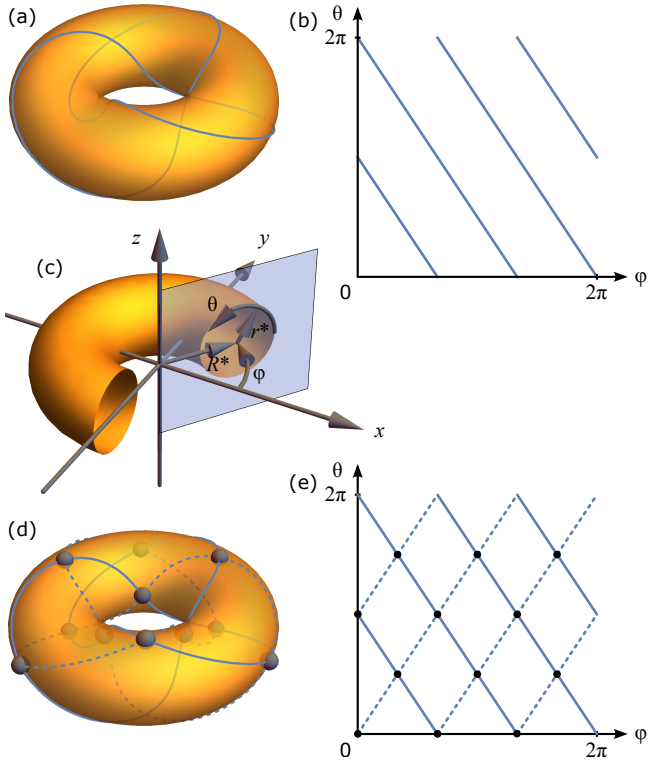

FIG. 1: Schematic of the construction of a regular array of dark spots on a torus. The construction is based on fields that contain vortex lines (blue lines) spiralling on the torus, performing m/n full turns of the poloidal angle, θ, during each turn of the toroidal angle, φ. The geometry of such a vortex line with $m = 3$ and $n = 2$ is shown schematically in 3D (a) and in a (θ, φ) plot of the torus surface (b). The poloidal angle θ and the toroidal angle φ themselves are shown in (c), together with the major and minor radii of the torus, R^* and r^*. Incoherent superposition of two fields containing different vortex lines spiralling on the same torus results in arrays of dark spots on the torus, specifically at the positions where the vortex lines in the two fields intersect. In the 3D plot shown in (d), the positions of the intersections of vortex lines in two fields, the first with parameters $m_1 = 3$, $n_1 = 2$, the second with $m_2 = -3$, $n_2 = 2$, are shown as grey spheres, in the (θ, φ) plot shown in (e) they are marked as black dots. Throughout, the vortex lines of the first field are shown as solid lines, those of the second field as dashed lines. The graphs were created with the help of the *Mathematica* notebook `topologyPlots.nb`, which is available in the supplementary material.

the vortex-line patterns appropriately, and which might themselves form interesting optical potentials. We then consider superpositions of two such fields in which different vortex lines of this kind spiral around a torus. We require the superposition to be incoherent so that the intensities add up, not the fields. At those positions where the vortex lines in the two fields intersect, i.e. where the intensities of both fields are individually zero, the combined intensity is also zero. In a plot of the torus surface that uses the toroidal angle, φ, and poloidal angle, θ, (Fig. 1(c)) as coordinates, these positions form approximately rectangular arrays on the torus (Fig. 1(d, e)).

Our construction is not diffraction-limited in the sense that it permits sub-wavelength trap separations. However, an experimental realisation of our construction will be challenging as the constructed fields contain a large range of relevant intensities. This would require very careful beam shaping: the trap structure is contained in the darker part of the beam, which is easily perturbed by stray light, for example light scattered from the much brighter parts of the beam. Giving the optical traps the required stiffness and depth might also require high laser powers. For sub-wavelength trap separations, a large intensity range is likely a fundamental feature of the field, but for larger separations there is no known fundamental reason why careful adjustment of the construction, for example starting from different vortex torus knots [14], should not lead to a drastic reduction in the intensity range; note, however, that devising and testing the required variations of the construction is a significant undertaking.

This paper is structured as follows. In section II we review the construction of monochromatic scalar fields that contain vortex lines lying on the surface of a distorted torus. We then show, in section III, how combinations of two such fields can result in rectangular arrays of dark optical traps on the surface of a distorted torus. In section IV, we discuss the adjustments required for our construction to work when polarisation is taken into account. In section V, we calculate, for one particular example, the standard parameters used to characterise trap arrays. Finally, we discuss details and the significance of this construction in section VI, before concluding (section VII).

II. SCALAR VORTEX LINES SPIRALLING ON A DISTORTED TORUS

Scalar vortex lines that form regular spirals on the surface of a distorted torus can be constructed in a number of ways. We review one way to create such fields [11], slightly varied in Refs [12, 13]; another way can be found in Ref. [14].

An optical vortex line, irrespective of its shape, is characterised by a phase change $m2\pi$ — m complete 2π phase cycles — encountered along a closed loop threaded by the vortex line. The "charge" m can be any integer, positive or negative. If a vortex line with charge $+1$ or -1 is perturbed with a small additional field, for example a uniform plane wave, it remains a vortex line with the same charge. In contrast, a charge-m vortex line, when perturbed splits into $|m|$ vortex lines with a charge of magnitude 1 and the same sign as m [15].

The construction of vortex lines that spiral on a torus starts with a field containing a charge-n vortex ring that is threaded by a charge-m vortex line (m and n are ar-

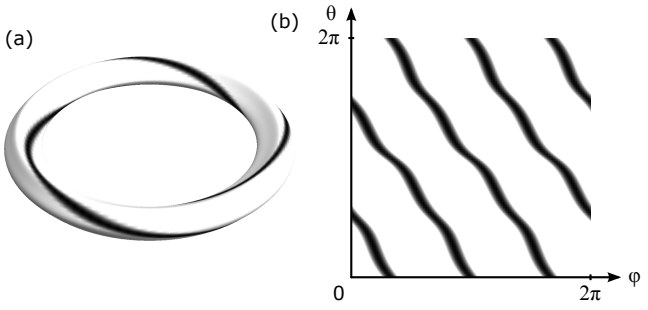

FIG. 2: Example of a scalar vortex line (black) spiralling on a distorted torus. The plots show the saturated intensity distribution on the torus, in 3D (a) and in the (θ, φ) coordinate system (b). The field was calculated following Ref. [11] for $m = 3$ and $n = 2$ and a perturbation amplitude $\varepsilon = 0.05$. Black represents intensity 0, white represents intensities ≥ 0.001. The graphs were created using the *Mathematica* notebook `geometryPlots.nb`, which is available in the supplementary material. The beam coefficients, and the way they were calculated, is outlined in App. A.

bitrary integers). When perturbed, the charge-n vortex ring splits into $|n|$ vortex lines with charge $+1$ or -1 lying on the surface of a distorted torus. The threading of the ring by a charge-m vortex line ensures that these vortex lines perform m full turns of the poloidal angle for each n turns of the toroidal angle.[27]

We now quantify this construction. We choose our coordinates such that the charge-n vortex ring lies in the plane $z = 0$, is centred on the origin and threaded by a charge-m vortex line along the z axis. In dimensionless cylindrical coordinates ($R \equiv kr$, φ, $Z \equiv kz$), where $k = 2\pi/\lambda$ is the wave number, such a field can be written in the form [11]

$$\psi_{m,n}(R, \varphi, Z) = \exp(\mathrm{i}m\varphi) F_{m,n}(R, Z), \tag{1}$$

where

$$F_{m,n}(R, Z) = \sum_{l=1}^{\frac{1}{2}n(n+1)} a_l J_m(b_l R) \exp\left(\mathrm{i}\sqrt{1 - b_l^2} Z\right), \tag{2}$$

where $J_m(x)$ is the mth-order Bessel function of the first kind, and the b_ls (which satisfy $|b_l| < 1$) and a_ls are dimensionless coefficients which depend on $|m|$, $|n|$, and the radius R^* of the initial charge-n vortex ring. Note that the field $\psi_{m,n}$ — like all fields in this paper — is dimensionless; the corresponding physical intensity can be obtained by multiplying the modulus squared of the field by a factor, A, with dimensions of intensity:

$$I = A|\psi|^2. \tag{3}$$

When adding a perturbation $\varepsilon\psi_p(R, \varphi, Z)$ to the field $\psi_{m,n}(R, \varphi, Z)$, a new field is created:

$$\Psi_{m,n}(R, \varphi, Z) = \psi_{m,n}(R, \varphi, Z) + \varepsilon\psi_p(R, \varphi, Z). \tag{4}$$

If the perturbation is chosen appropriately, for example if it is chosen to be a small-amplitude uniform plane wave, this field contains the desired vortex line(s) spiralling on a distorted torus with major radius R^*. Fig. 2 shows the theoretically calculated intensity on the distorted torus for one example of such a field.

We stress that the torus is distorted. The vortex lies on a surface where the intensity of the unperturbed field equals that of the perturbation, and where the phases of these two fields differ by π. We use a plane-wave perturbation of the form

$$\psi_p(R, \varphi, Z) = \exp(\mathrm{i}Z), \tag{5}$$

and so the unfolded vortex lines lie on a surface where the intensity of the unperturbed field equals $|\varepsilon|^2$. As the intensity of the unperturbed field depends on the poloidal direction, the resulting torus will be distorted, generally more so with increasing magnitude of the perturbation. This distortion can clearly be seen in Fig. 2; its effect in the (θ, φ) plot is that the vortex lines are not straight. The distortion depends on the values of $|m|$ and $|n|$.

III. ARRAYS OF DARK SPOTS ON A DISTORTED TORUS

Now consider a superposition of two fields, Ψ_{m_1,n_1} and Ψ_{m_2,n_2}, each described by Eqn (4), with the parameters chosen such that both fields contain vortex lines spiralling on the same torus. We consider both coherent and incoherent superpositions, for reasons that will become clear later. Where the vortex lines intersect, the intensity is zero, and as the vortex lines form approximately regular spirals on the torus, these positions of zero intensity form an approximately regular array on the torus (Fig. 1(d,e)). Using different combinations of the values of m_1, n_1, m_2 and n_2, different arrays can be created, as schematically illustrated in Fig. 3. If the frequency of the light is chosen appropriately, the zero-intensity positions — provided they are completely surrounded by non-zero intensity — can form blue-detuned traps for atoms.

The relationship between the parameters m_1, n_1, m_2, n_2 and the number of traps in the array can be understood as follows. In a (θ, φ) plot, a vortex line with parameters m and n forming a regular spiral is a straight line, which can be parametrised in the following way:

$$\theta = \frac{m}{n}\varphi + 2\pi\frac{q}{n}, \tag{6}$$

where q is an integer. The optical traps are created at those positions where the vortex lines intersect, i.e. positions which satisfy the condition

$$\frac{m_1}{n_1}\varphi + 2\pi\frac{q_1}{n_1} = \frac{m_2}{n_2}\varphi + 2\pi\frac{q_2}{n_2}. \tag{7}$$

This equation has the solution

$$\varphi = 2\pi\frac{q_2 n_1 - q_1 n_2}{m_1 n_2 - m_2 n_1}. \tag{8}$$

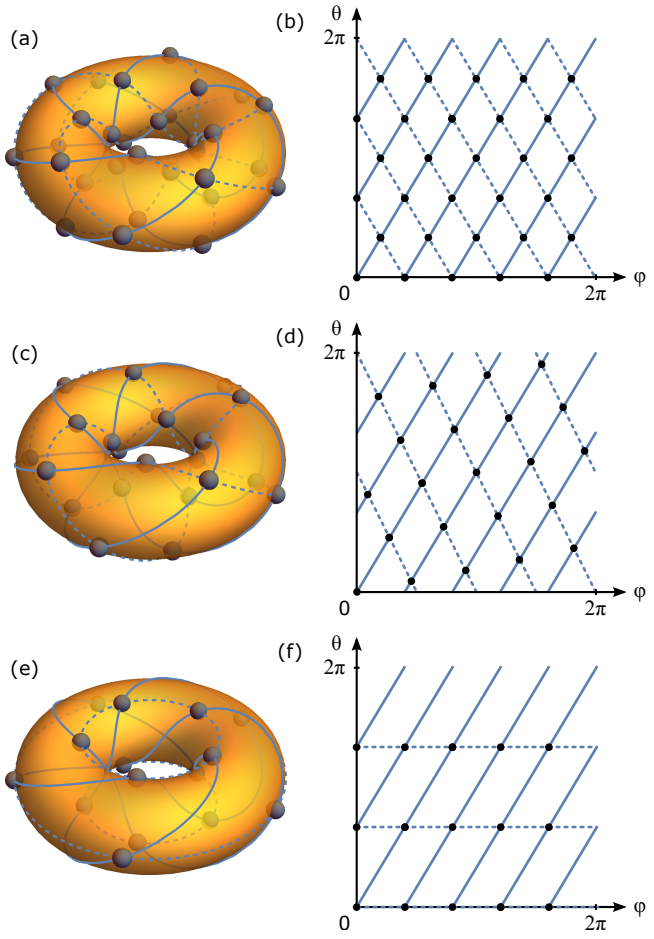

FIG. 3: Arrays of dark spots resulting from different parameter choices. (a,b) Face-centred rectangular array, shown for the case $m_1 = 5$, $n_1 = 3$, $m_2 = -5$, $n_2 = 3$; (c,d) skew array ($m_1 = 5$, $n_1 = 3$, $m_2 = -4$, $n_2 = 2$); (e,f) rectangular array ($m_1 = 5$, $n_1 = 3$, $m_2 = 0$, $n_2 = 3$). The graphs were created with the help of the *Mathematica* notebook `topologyPlots.nb`, which is available in the supplementary material.

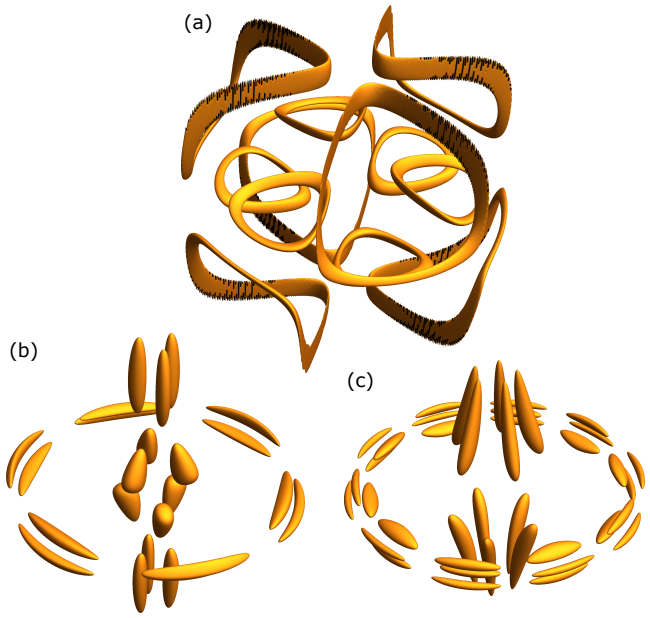

FIG. 4: Contour plots of the intensity in the coherent superposition of $\Psi_{3,2}$ and $\Psi_{-3,2}$ (a) and in incoherent superpositions of the fields $\Psi_{3,2}$ and $\Psi_{-3,2}$ (b) and $\Psi_{5,3}$ and $\Psi_{-5,3}$ (c). The plots show contours with intensity 0.001 in the arbitrary units used in all simulations in this paper. (a) In the coherent superposition of the fields $\Psi_{3,2}$ and $\Psi_{-3,2}$, the dark regions in the beam do not form the desired structure. (b,c) In the incoherent superpositions, the intensity zeros on the torus are surrounded by approximately ellipsoidal low-intensity surfaces that can clearly be seen to form the desired regular array on a torus. Additional intensity zeros formed by intersections of the threading vortex lines can be seen around the torus axis. The size of the perturbation was chosen to be $\varepsilon = 0.05$ in (a) and (b), and $\varepsilon = 0.025$ in (c). The plots were created using the *Mathematica* notebook `geometryPlots.nb`, available in the supplementary material.

As the toroidal angle φ lies in the range $[0; 2\pi)$, the value of the fraction on the RHS of Eqn (8) is within the range $[0, 1)$. For any given set of values of m_1, n_1, m_2 and n_2 there are $N = |m_1 n_2 - m_2 n_1|$ values of $\varphi \in [0; 2\pi)$ satisfying this requirement, and therefore there are N traps. For example, in the array shown in Fig. 3(c,d), Eqn (8) correctly gives the trap number as $N = 22$.

It is natural first to consider a coherent superposition of the fields Ψ_{m_1,n_1} and Ψ_{m_2,n_2}. However, numerical simulations such as the one shown in Fig. 4(a) demonstrate that the interference between the fields does not give the intended result: instead of an array of optical traps on a torus, the superposition contains a complex 3D structure of dark loops.

This interference can be avoided by superposing the two fields incoherently, such that their intensities add. Experimentally, this could be achieved by making the frequencies of the two fields (slightly) different; by making the fields' polarisations different; or by forming both fields from different parts of the same beam while ensuring that they have propagated through distances that differ by more than the beam's coherence length. The combined intensity of the two perturbed fields, Ψ_{m_1,n_1} and Ψ_{m_2,n_2}, defined in Eqn (4), is then

$$I = |\Psi_{m_1,n_1}|^2 + |\Psi_{m_2,n_2}|^2 . \qquad (9)$$

Fig. 4(b,c) shows contour plots of the intensity in such incoherent beam superpositions, calculated according to Eqn (9). The intensity of the contours was chosen to be just below that separating neighbouring traps. Each contour surface surrounding one of the intensity zeros on the distorted torus can be seen to form a closed, approximately ellipsoidal, surface, demonstrating that each intensity zero is surrounded by non-zero intensity in all directions. Note that the approximately ellipsoidal shape of the low-intensity contours is consistent with anisotropic,

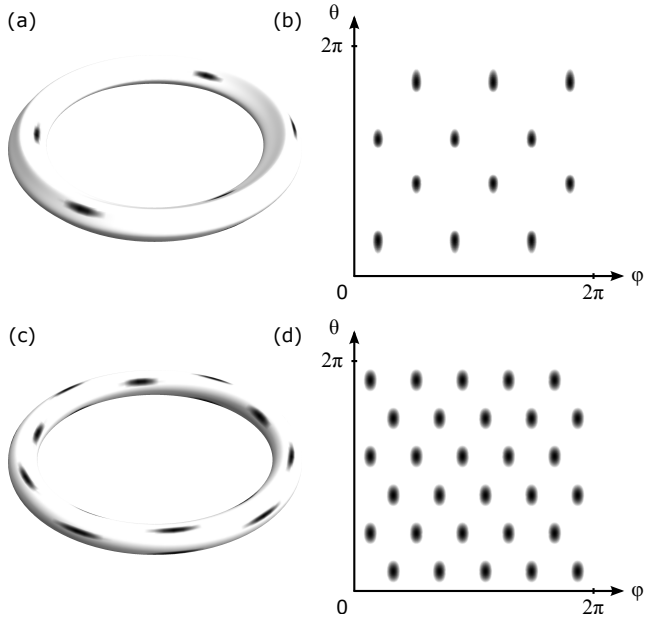

FIG. 5: Intensity on the distorted torus in incoherent superpositions of the fields $\Psi_{3,2}$ and $\Psi_{-3,2}$ (a,b) and $\Psi_{5,3}$ and $\Psi_{-5,3}$ (c,d). The plots on the left (a, c) show the distorted torus in 3D, those on the right (b, d) show the (θ, φ) plane. The dark spots coincide with the positions where vortex lines from the two fields intersect. Fig. 4(b,c) shows contour plots for the same superpositions, but note that the viewpoints of those plots subtly differ from those used in the 3D plots (a) and (c), resulting in the trap arrays appearing shifted. The intensity range plotted is from 0 to 0.001 in the arbitrary units used throughout this paper. The basic plots were created with the *Mathematica* notebook `geometryPlots.nb`, which is available in the supplementary online material.

approximately harmonic, dark traps. Fig. 5 shows the intensity on the surface of the relevant distorted torus for the same fields. The intensity plots in the (θ, φ) coordinate system show the regularity of the trap array in both cases. In App. B (Eqn (B7)) it is shown that, in the case of a plane-wave perturbation $\varepsilon\psi_p = \varepsilon \exp(\mathrm{i}k_z z)$, neighbouring traps are separated by a barrier intensity $I_b = 2A|\varepsilon|^2$. We will consider the important question of the length scale of the trap arrays later, in Sec. VI.

IV. EXTENSION TO VECTOR BEAMS

Our construction so far gives the "nicest" tori, i.e. the tori with the closest-to-circular toroidal cross-sections, if the beams are tightly focussed. But tightly focussed beams can possess a sizeable longitudinal component of the electric and magnetic field, which contributes to the intensity and therefore has the potential to destroy the carefully crafted intensity minima associated with the transverse components. It is therefore important to consider effects due to the vector character of the field.

Simulations (not shown) of the beams discussed in the previous sections which have been modified to be linearly polarised reveal that the intensity associated with the longitudinal component can indeed destroy the traps. Our solution is to construct the undisturbed vortex ring, which in the scalar case (Eqn (2)) consists of (non-diffracting) scalar Bessel beams, from non-diffracting vector beams whose polarisation is chosen such that its longitudinal component is zero irrespective of focussing, as follows.

We start with non-diffracting solutions to the Helmholtz equation of the form [16]

$$U^R = -\mathrm{i}a \exp\left(\mathrm{i}\sqrt{1-b^2}Z\right) \times \times \sum_l \exp(\mathrm{i}l\varphi) \left[\alpha_{l+1}^{(+)} \mathrm{e}^{\mathrm{i}\varphi} + \alpha_{l-1}^{(-)} \mathrm{e}^{-\mathrm{i}\varphi}\right] J_l(bR), \tag{10}$$

$$U^\varphi = a \exp\left(\mathrm{i}\sqrt{1-b^2}Z\right) \times \times \sum_l \exp(\mathrm{i}l\varphi) \left[\alpha_{l+1}^{(+)} \mathrm{e}^{\mathrm{i}\varphi} - \alpha_{l-1}^{(-)} \mathrm{e}^{-\mathrm{i}\varphi}\right] J_l(bR), \tag{11}$$

$$U^Z = -\frac{2a^2}{\sqrt{1-b^2}} \exp\left(\mathrm{i}\sqrt{1-b^2}Z\right) \times \times \sum_l \exp(\mathrm{i}l\varphi) \left[\alpha_l^{(+)} - \alpha_l^{(-)}\right] J_l(bR), \tag{12}$$

where (U^R, U^φ, U^Z) are the vector components of the complex amplitude of the electric field, $a, b, \alpha_i^{(+)}, \alpha_i^{(-)}$ are constants and $J_l(x)$ is an l-th order Bessel function of the first kind.

To eliminate the longitudinal component U^Z of the field everywhere, we have to choose $\alpha_l^{(+)} = \alpha_l^{(-)}$. The easiest choice is then $\alpha_l^{(+)} = \alpha_l^{(-)} = \delta_{lm}$, where δ_{lm} is the Kronecker delta. With the choice $a = 1$, the resulting transversally polarized vector beam is then of the form

$$\vec{U} = \exp(\mathrm{i}m\varphi) \exp\left(\mathrm{i}\sqrt{1-b^2}Z\right) \vec{J}_m(bR), \tag{13}$$

where the radial, azimuthal, and longitudinal components of the vector function $\vec{J}_m(bR)$ are

$$J_m^R(bR) \equiv -\mathrm{i}\left[J_{m-1}(bR) + J_{m+1}(bR)\right], \tag{14}$$

$$J_m^\varphi(bR) \equiv J_{m-1}(bR) - J_{m+1}(bR), \tag{15}$$

$$J_m^Z(bR) \equiv 0. \tag{16}$$

Note that the sum of the Bessel functions in the radial component J_m^R becomes zero only in the case $m = 0$, which means that we can obtain a purely azimuthally polarized beam if and only if $m = 0$.

The construction of scalar vortex lines spiralling on a distorted torus started with a field $\psi_{m,n}$ containing a charge-n vortex ring (Eqn (1)). This field is a superposition of scalar Bessel beams, each of the form

$$\exp(\mathrm{i}m\varphi) \exp\left(\mathrm{i}\sqrt{1-b^2}Z\right) J_m(bR). \tag{17}$$

Our strategy for extending the construction to vector fields is to replace these scalar Bessel beams with corresponding vector fields given by Eqn (13), i.e. by replacing the scalar (Bessel) function $J_m(bR)$ with the vector function $\vec{J}_m(bR)$. The scalar field $\psi_{m,n}$ then becomes the vector field $\vec{\psi}_{m,n} = (\psi^R_{m,n}, \psi^\varphi_{m,n}, 0)$, where

$$\psi^R_{m,n} = -\mathrm{i} \sum_{l=1}^{\frac{1}{2}n(n+1)} a_l \exp(\mathrm{i}m\varphi) \exp\left(\mathrm{i}\sqrt{1-b_l^2}Z\right) \times \times \left[J_{m-1}(b_l R) + J_{m+1}(b_l R)\right], \tag{18}$$

$$\psi^\varphi_{m,n} = \sum_{l=1}^{\frac{1}{2}n(n+1)} a_l \exp(\mathrm{i}m\varphi) \exp\left(\mathrm{i}\sqrt{1-b_l^2}Z\right) \times \times \left[J_{m-1}(b_l R) - J_{m+1}(b_l R)\right]. \tag{19}$$

We require both the radial and azimuthal component of this vector field to contain coinciding charge-n vortex rings, both of radius R^*. This condition implies the second modification of the procedure presented in Ref. [11]: the condition for the existence of a charge-n vortex ring of radius R^* in the $Z = 0$ plane, which is equivalent to Eqn (2.5) in Ref. [11], has to be satisfied for both fields $\psi^R_{m,n}$ and $\psi^\varphi_{m,n}$ simultaneously. This leads to a set of $n(n+1)$ equations — twice as many as in the case of scalar fields. To make this new bigger system of equations regular, we treat the coefficients b_l, which were chosen arbitrarily in Ref. [11], as unknown variables.

To the field $\vec{\psi}_{m,n}$, a small perturbation $\varepsilon\vec{\psi}_p$ with an appropriate polarisation is added, leading to a new field

$$\vec{\Psi}_{m,n} = \vec{\psi}_{m,n} + \varepsilon\vec{\psi}_p. \tag{20}$$

In our simulations, we use the azimuthally polarised, non-diffracting, perturbation field $\varepsilon\vec{\psi}_p$ with

$$\vec{\psi}_p = \left(0, \frac{J_1(b_p R)}{J_1(b_p R^*)} \exp\left(\mathrm{i}\sqrt{1-b_p^2}Z\right), 0\right), \tag{21}$$

where b_p has been chosen such that the first maximum of $J_1(b_p R)$ is at $R = R^*$. This field $\vec{\psi}_p$ is actually the field $\vec{\psi}_{0,1}$, normalised such that the amplitude at $(R, Z) = (R^*, 0)$ equals 1. Note that this field $\vec{\psi}_p$ does not perturb the radially polarised field, which keeps its charge-n vortex ring. The perturbation amplitude ε of the azimuthally polarised component is chosen such that the distorted torus on which the vortex lines spiral stays within the dark part of the radially polarised component.

The field containing optical traps is then obtained by the incoherent superposition of the fields $\vec{\Psi}_{m_1,n_1}$ and $\vec{\Psi}_{m_2,n_2}$. Fig. 6 shows an example for $m_2 = -m_1$ and $n_2 = n_1$, calculated without any approximations. The traps can be clearly seen to have the desired configuration.

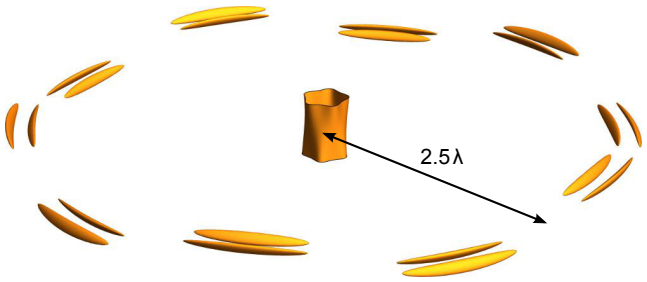

FIG. 6: Intensity contour of the field $|\vec{\Psi}_{5,2}|^2 + |\vec{\Psi}_{-5,2}|^2$. The field contains intensity minima in the desired configuration. The plots show contours with intensity 5×10^{-4}. In comparison, the maximum intensity in the beam is approximately 17 (see Fig. 11). The coefficients a_l, b_l of the unperturbed beams are listed in App. A, the perturbation amplitude is $\varepsilon = 2 \times 10^{-2}$.

V. EXAMPLE

For one particular example, we calculate here the parameters used in the literature to characterise the trap lattice. We consider the case of ^{85}Rb atoms where our light field excites, off-resonantly, the $5^2S_{1/2} - 5^2P_{3/2}$ transition. We use atomic data from Ref. [17]. The detuning is chosen to be $\Delta = 100\,\Gamma$. The wavelength of the light is $\lambda = 780.24\,\mathrm{nm}$, the excited state spontaneous emission rate is $\Gamma = 5.98 \times 2\pi\,\mathrm{MHz}$, while the saturation intensity for the selected atomic transition is $I_s = 16.2\,\mathrm{W/m^2}$. The interaction is characterised by a recoil angular frequency $\omega_{\mathrm{rec}} = 3.83 \times 2\pi\,\mathrm{kHz}$ and a corresponding recoil energy $E_{\mathrm{rec}} = \hbar^2k^2/2M = 2.54 \times 10^{-30}\,\mathrm{J}$.

We assume that the atoms trapped in our toroidal lattice are two-level systems and the optical dipole potential is due to the AC Stark shift and therefore proportional to the intensity, while in the case of a relatively large detuning it is also independent of polarization. We further assume that locally the trapped atoms are at the ground state of a three-dimensional, non-isotropic, simple harmonic potential, and that they are well localised around the trap minimum; we can safely say that these assumptions are justified for $I_b/I_s \geq 60$. In this case, the atomic wave function plays the role of the Wannier wave functions localized in a particular potential well.

An individual trap is often characterised by its depth, here measured by the barrier potential between neighbouring traps, U_b, and the trap frequencies, ω, which are the oscillation frequencies of trapped atoms in different directions and a measure of a trap's stiffness. For atoms trapped in a lattice of traps, of particular importance are the hopping rates, J, which describe tunneling between adjacent trapping sites, and the on-site collision rate, C, which describes the strength of the interactions between the atoms trapped in the same trap.

The trap frequencies were calculated from the second derivatives of the dipole potential, which in turn were calculated from the second directional derivatives of the

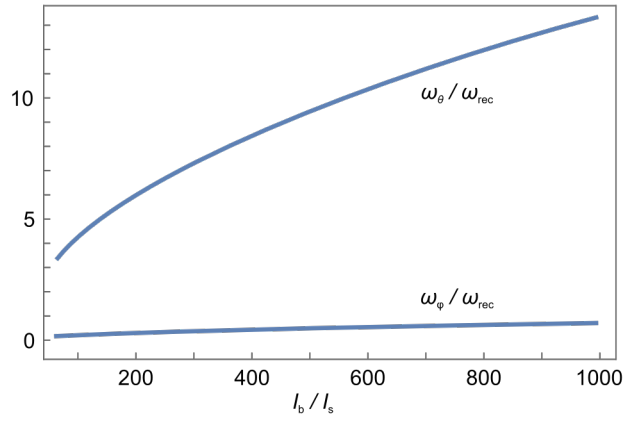

FIG. 7: Ground-state trapping angular frequencies in the toroidal and poloidal directions in units of the angular recoil frequency against the light-field intensity.

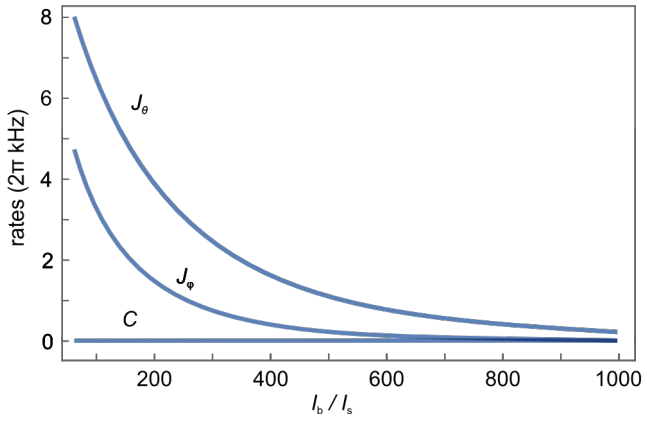

FIG. 8: Hopping rates in the poloidal direction, J_θ, and in the toroidal direction, J_φ, and the on-site collision rate, C, plotted against the intensity. The graphs were calculated for trapped ^{85}Rb atoms and a detuning $\Delta = 100\,\Gamma$.

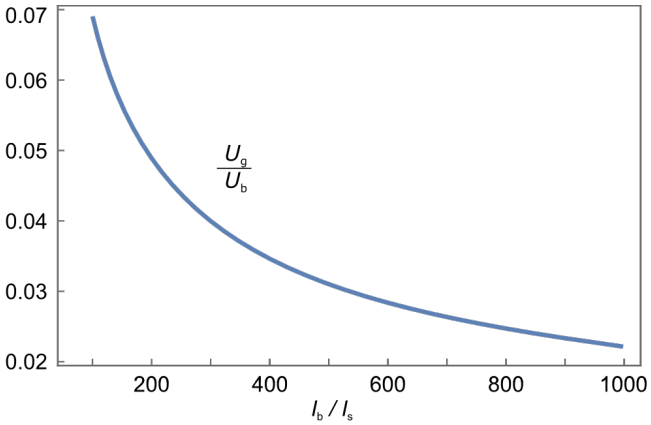

FIG. 9: Ratio of ground-state energy, U_g, and the maximum potential well optical-dipole potential energy, U_b, plotted against the intensity.

intensity at the centre of one of the traps in the toroidal, poloidal, and radial directions. We did this calculation for the intensity $|\vec{\Psi}_{5,2}|^2 + |\vec{\Psi}_{-5,2}|^2$. The second directional derivative in the direction of the vector $\mathbf{v}$ is given by $D^2_{\hat{\mathbf{v}}} I = \hat{\mathbf{v}}^\top \mathbf{H} \hat{\mathbf{v}}$, where $\mathbf{H}$ is the Hessian matrix of I, calculated at the trap centre. These are $D^2_{\hat{\boldsymbol{\Phi}}} I = 0.1625\, I_b k^2$, $D^2_{\hat{\boldsymbol{\theta}}} I = 57.50\, I_b k^2$, $D^2_{\hat{\mathbf{r}}} I = 12.875\, I_b k^2$, where $I_b = 2A|\varepsilon|^2$ is the intensity barrier between the traps (see Eqn (B7)) and $k = 2\pi/\lambda$ is the wave number, as before. The trap frequencies are simply the resonance frequencies of the harmonic potential; we plot these for a range of light-field intensities (which correspond to different values of A) in Fig. 7.

We calculate the hopping rates from the overlap integral of the Wannier wave functions, $w(\vec{r} - \vec{r}_i)$ and $w(\vec{r} - \vec{r}_j)$, corresponding to two neighbouring trapping sites, i and j:[1]

$$J = \int \mathrm{d}^3 r w^*(\vec{r} - \vec{r}_j) \left(-\frac{\hbar^2}{2m} \nabla^2 + V(\vec{r}) \right) w(\vec{r} - \vec{r}_i). \quad (22)$$

The collision rate was calculated using the equation

$$C = \frac{4\pi\hbar^2 a}{m} \int \mathrm{d}^3 r \, |w(\vec{r} - \vec{r}_i)|^4 \quad (23)$$

(Eqn (26.18) in Ref. [1]), where a is the scattering length. The value for a has been taken from Ref. [18]. A plot of the hopping rates and the collision rate against light-field intensity is shown in Fig. 8. We clearly see that for low intensities the collision rate is far smaller than the hopping rates. The dipole trapping potential increases linearly with the intensity from zero up to $1800\, E_{\mathrm{rec}}$ as the intensity I_b varies from $60\, I_s$ to $1000\, I_s$, and we see in Fig. 9 that it remains far deeper than the energy of the ground state. All the above ensure that our scheme is capable for atom trapping at moderate intensities. We also see that the hopping rates in the toroidal and poloidal directions are of comparable size, with the first being always smaller in size. The same conclusion is true for the ground-state trapping frequencies. When a Bose-Einstein condensate is loaded in an optical lattice, it provides an ideal environment for the exhibition of the transition from the regime of the superfluidity to that of Mott insulator. The crucial parameter is the relation of the size of the hopping rates to that of the on-site two-body interactions. As our numerical calculations have shown, for our toroidal lattice the hopping rates remain far stronger for a broad range of intensities and detunings, which indicates that tunnelling is dominant over inter-particle interactions.

Comparing the hopping rates with the collision rate, all shown in Fig. 8, we clearly see that tunneling is dominant over inter-particle interactions for the intensity values for which the simple harmonic approximation is valid. The hopping rates are also dominant over the photon-scattering rate, which can be seen as follow. The photon-scattering rate for an atom trapped in a dipole trap is

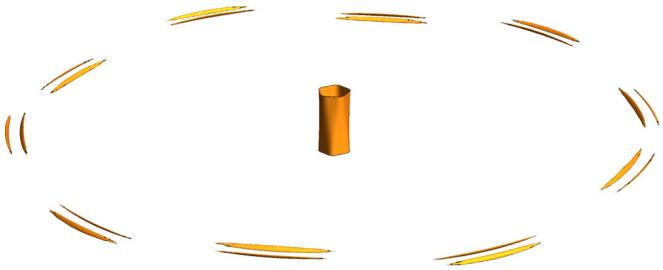

FIG. 10: Same as Fig. 6, but with each vector Bessel beam replaced by a numerical approximation of a corresponding vector Bessel-Gauss beam (see App. C). The intensity minima still possess the desired configuration. The surface shown is the contour with intensity 5×10^{-4}; the maximum intensity in the beam is ≈500.

defined (Eqn (29) in [19]) by the relation

$$\Gamma_{\rm sc} = \frac{\Gamma}{\hbar\Delta}\left(U_0 + \frac{3}{2}k_B T\right), \tag{24}$$

where U_0 is the dipole potential at the center of the trap and T is the trapped sample temperature. For a blue-detuned (dark) trap, $U_0 = 0$. For a BEC of Rb atoms there have been reported temperatures up to 20 nK (JILA) [20]. Putting these numbers into the above equation results in a photon-scattering rate

$$\Gamma_{\rm sc} = 6 \times 10^{-4} \times 2\pi\,{\rm kHz}, \tag{25}$$

which is far smaller than the hopping rates shown in Fig. 8.

An important parameter is the laser-beam power required to create a suitable array of traps. In our construction, we use (vector) Bessel beams, which are idealisations that are unbounded and possess infinite power. Clearly, these cannot be created experimentally; in experiments, Bessel beams are therefore usually replaced by Bessel-Gauss beams [21], which are Bessel beams modulated by a Gaussian envelope, and which have finite power. The wider the Gaussian envelope, the more similar the Bessel-Gauss beam is to the corresponding Bessel beam; in the limit of an infinitely wide Gaussian envelope, the two beams are the same. Similarly, vector Bessel beams can be replaced by vector Bessel-Gauss beams in our construction. For sufficiently wide Gaussian envelopes, the construction will still work, that is, the array of traps will have the desired geometry.

We have studied one particular example of a beam in which this replacement has been made. Fig. 10 shows the simulated intensity contour in a field that is the same as that shown in Fig. 6 other than that each vector Bessel beam has been replaced by a corresponding vector Bessel-Gauss beam (App. C). The geometry of the contour has changed slightly; this is related to the fact that we chose to simulate a relatively narrow Gaussian envelope, and that we replaced each vector Bessel beam with a Bessel-Gauss beam of greater amplitude without a corresponding increase in the size of the perturbation. Most importantly, however, the traps retain the desired configuration. Numerical integration of the intensity over the plane $z = 0$ yields a beam power of $P = 55,500Ak^{-2}$. For the specific choice $k = 2\pi/\lambda = 8.053 \times 10^6\,{\rm m}^{-1}$ and $A = 2.03 \times 10^7\,{\rm W/m}^2$ (corresponding to a barrier intensity $I_b = 2A|\varepsilon|^2 = 16200\,{\rm W/m}^2 = 1000\,I_s$, where $I_s = 16.2\,{\rm W/m}^2$), the beam power is 17.3 mW, which is easily achievable in experiments.

VI. DISCUSSION

For applications in atomic physics, the scaling of the torus is important. At first, it seems clear that the torus could simply be imaged with a magnification other than 1 to change its size. However, as discussed in App. D, imaging of a Bessel beam with a transverse magnification $M \neq \pm 1$ scales the beam longitudinally by a different magnification factor. This means that isotropic scaling of the knot field is not possible by imaging. Furthermore, transverse scaling by $M \neq \pm 1$ of non-paraxial Bessel-beam superpositions results in different Bessel-beam components being scaled by different longitudinal scaling factors, which means that the superposition is not simply stretched in the longitudinal direction, but changes shape and, in the case of our knot fields, the trap configuration.[28] The major radius of the torus, R^*, can therefore be scaled only by changing the wave number, k; for a given k, R^* is fixed by the set of equations for the parameters of the initial, unperturbed, vortex-ring field; this set of equations is solved numerically in App. A. (Of course, there might be other solutions of these (non-linear) equations, with different torus dimensions.) For vector beams $\vec{\Psi}_{\pm5,\pm2}$, $kR^* \approx 16$ (see Table II), which implies $R^* \approx 2.5\lambda$. Similarly, in the beams $\vec{\Psi}_{\pm3,\pm2}$, $R^* \approx 2.4\lambda$, and in the beam $\vec{\Psi}_{\pm5,\pm3}$, $R^* \approx 15\lambda$. The minor torus radius, r^*, can be scaled by changing the amplitude of the perturbation (see Appendix B, specifically Eqn (B5)). In principle, this enables r^* to be arbitrarily small.

It is worth stressing that our construction is not diffraction-limited, as the separation between neighbouring traps in the array can, in principle, be arbitrarily small, which is important as it enables interactions between atoms trapped in neighbouring sites to be maximised and a wider parameter space to be explored. This is true both in the toroidal direction and in the poloidal direction: the vortex separation in the toroidal direction can be reduced by increasing the value of m, which, at least in principle, is unlimited; the vortex separation in the poloidal direction can be reduced either by increasing the (again in principle unlimited) value n, or by decreasing the minor radius of the torus, r^*.

Vortex knots have been created experimentally before [12, 13]. Those experiments concentrated on the topology of the knots. The geometry differed significantly from that required here: the knots were on a significantly

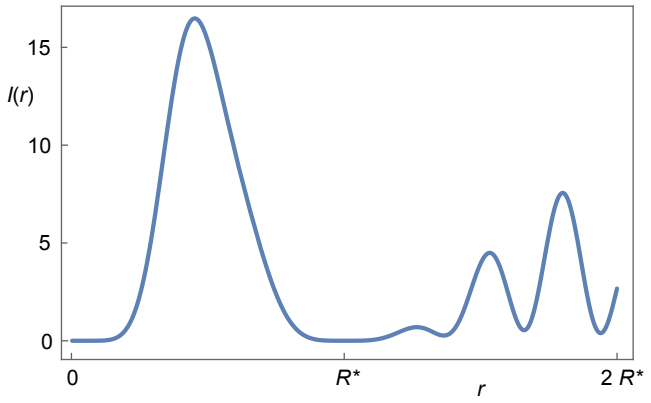

FIG. 11: Radial intensity distribution of the incoherent superposition of $\vec{\Psi}_{5,2}$ and $\vec{\Psi}_{-5,2}$ along the line $z = 0$ and $\varphi = 0$. The intensity is shown in the same arbitrary units used in Fig. 6.

larger scale; and they were heavily distorted. Trap arrays constructed from such vortex knots would therefore be too large and irregular to realise the theoretical ideas discussed here, but greater care with the beam preparation might be able to ameliorate these problems.

If the trap separation is required to be small, even sub-wavelength, then there is another, possibly more significant, problem: the maximum intensity in the beam significantly outweighs that in the trap region. This can be seen by comparing the maximum intensity in the beam to the intensity separating neighbouring traps. The latter is given by $2\varepsilon^2$, which is of order 4×10^{-4} in the example shown in Fig. 6, for which the former is ≈ 17 (Fig. 11), so the maximum intensity in the beam is $\approx 4.2 \times 10^4$ times greater than the intensity separating neighbouring traps. Note that the maximum intensity in the beam depends very much on the beam; for example, for the incoherent superposition of the scalar functions $\Psi_{3,2}$ and $\Psi_{-3,2}$ it is ≈ 60 in the $z = 0$ plane, but for the incoherent superposition of $\Psi_{5,3}$ and $\Psi_{-5,3}$ it is $\approx 3 \times 10^{11}$. For possible experimental realisations this means that the presence of any additional field in the trap region with an intensity that is tiny compared to the maximum intensity in the beam but still greater than that separating the traps destroys the desired intensity structure. Great care must therefore be taken to avoid creating such additional fields; for example, if the beam is created holographically, such additional fields could be due to light from different diffraction orders, or due to effects such as pixellation or phase error.

Greater care still must be taken when the separation between neighbouring traps becomes smaller, especially when utilising the attractive feature of our construction that the separation between neighbouring traps is not diffraction-limited: this is the realm of superoscillations, and as superoscillations with higher spatial frequencies tend to occur in the darker part of the field [22, 23], smaller trap separations are likely to be associated with large intensity ratios in the beam. This can be seen in the case of the $|n|$ traps whose positions differ only in their poloidal angle (i.e. whose positions have the same toroidal angle, and which therefore lie on the same radial slice), which are separated by an intensity barrier of height I_b that scales with the separation s between neighbouring traps as $I_b \propto s^{2n}$ (App. B).

We stress here that we see our construction as a starting point of a process that will hopefully result in an easier-to-realise beam. One possible avenue for making it easier to realise optical potentials with a similar topology is to consider using other fields containing torus-knot vortices as the basis of our construction, in the hope that these might have a greater ratio between the intensity separating the traps and the maximum intensity in the beam, and generally be easier to realise. Here we use the superposition of Bessel beams from Ref. [11]; it is also possible to consider a similar construction that uses superpositions of Laguerre-Gauss beams [12], and it might be possible to use other beam families, for example the modes of cylindrical waveguides, whose power is spread only over the cross-section of the waveguide instead of an infinite plane (like in the Bessel beams), and which therefore potentially require much less powerful laser beams to achieve the same light distribution. There are also completely different — and arguably simpler — constructions that result in non-threaded knots [14].

In this paper, we have (mostly) discussed combinations of fields with the same values of n and the same absolute values of m. In this particular case, the spiralling vortex lines lie on the same distorted torus. On the other hand, if we want to achieve more general geometries of a trap distribution, two different sets (m_1, n_1) and (m_2, n_2) are needed. Fig. 3(c-f) shows examples of the types of arrays that can be achieved in this way. Specifically, frames (e) and (f) demonstrate that it is possible to obtain a rectangular array in φ and θ by combining a field with m_1 and n_1 with another with $m_2 = 0$ and $n_2 = n_1$.

However, in that case, the vortex lines spiral on different distorted tori. This then means that the vortex lines no longer necessarily intersect. But they *can* intersect: the two different distorted tori certainly can intersect, and if it can be arranged that the vortex lines on both tori pass through the positions where the tori intersect then the vortex lines also intersect exactly. Clearly, this places significant conditions on the construction. If exact intersection of the vortex lines cannot be achieved then the tori can be made as similar as possible, such that the vortex lines — wherever they are on those tori — intersect at least approximately, resulting not in intensity *zeros* but *minima* that can still form optical traps. This approach requires scaling of one light field relative to the other which, as discussed above (and in Appendix D), is possible only within tight limitations.

VII. CONCLUSIONS

We have described, theoretically, a scheme to create arrays of dark traps which are, in principle, very interesting to atom optics. A particularly salient feature of the fields is that the arrays of dark spots are not diffraction-limited: the period of the arrays can be, at least in principle, deeply sub-wavelength. However, it will be challenging to generate these arrays experimentally.

Our toroidal scheme is a first step towards the experimental generation of a toroidal optical lattice for atoms. The trapping of atoms in such a lattice would be an ideal environment for simulating the FQHE. Hopping of atoms between trapping sites in the poloidal and the toroidal directions will simulate the magnetic fluxes on the surface and inside the torus. The fact that these trapping sites which correspond to light intensity minima can come arbitrarily close to each other favours the achievement of very large magnetic fluxes. In our toroidal light field there are dark trapping sites where blue-detuned traps confine atoms at a local minimum of the optical intensity. As it is known dark trapping reduces photon scattering and light shifts, and is of particular interest for experiments using Rydberg atom excitation because blue detuned configurations allow for simultaneous trapping of both ground and Rydberg excited states [24]. A further careful analysis though is required regarding the properties of the trapping in our toroidal lattice. Parameters like the maximum achievable potential depth, the fluctuations of the dipole forces responsible for trapping, the average photon scattering rate and the collision rates have to be carefully examined, using in the calculations experimental values that have been used in atom dipole experiments of different atomic species. Note that the example presented in Sec. V covers only a tiny subset of the vast parameter space to be explored in actual experimental implementations. Technical problems, like the loading of pre-cooled atoms at the toroidal lattice trapping sites is also another important issue that has to be considered in case of an experiment.

Finally, our work highlights the interactions of crossing vortex lines in superposed fields, and provides motivation for studying them further.

VIII. ACKNOWLEDGEMENTS

The authors acknowledge extremely useful discussions with Peter Zoller (Innsbruck), Danica Sugic and Mark Dennis (Bristol), with Kevin O'Holleran (Cambridge), and with Neal Radwell and Sonja Franke-Arnold (Glasgow). This project was supported by King Saud University, Deanship of Scientific Research, College of Sciences Research Center. JB acknowledges an Erasmus+ studentship and a PhD studentship, funded by the UK's Engineering and Physical Sciences Research Council (EPSRC, grant number EP/N/509668/1).

Appendix A: Beam coefficients

$(\|m\|,\|n\|)$	(3,2)	(5,3)
kR^*	5.44992	7.52597
a_1	1	1
a_2	10.0302	−1073621
a_3	−3.1896	84311.3
a_4		−10978.4
a_5		1288.76
a_6		−90.1129
b_1	1	1
b_2	1/3	1/6
b_3	2/3	2/6
b_4		3/6
b_5		4/6
b_6		5/6

TABLE I: Beam coefficients for the scalar beams shown in Figs 2, 4, and 5.

The coefficients for scalar beams (sections II and III) were calculated using the procedure described in Ref. [11], as follows. Firstly, the coefficients $b_l \leq 1$ were arbitrarily chosen to be uniformly distributed across the interval [0,1]. The coefficient a_1 was chosen to be equal to one, and the set of $\frac{1}{2}n(n+1)$ equations

$$\partial_r^q \partial_z^{p-q} \psi_{m,n}(r,0,z)\big|_{r=R^*,z=0} = 0, \tag{A1}$$

where $p = 0,1,...,n-1$ and $q = 0,1,...,p$, was solved numerically, using *Matlab*, for the variables $\{kR^*, a_2, a_3, ..., a_{\frac{1}{2}n(n+1)}\}$. Table I lists the resulting beam coefficients.

The coefficients for vector beams (section IV) were calculated using the following variation of the above procedure. The coefficient a_1 was again chosen to be equal to one, and the set of $n(n+1)$ equations

$$\partial_r^q \partial_r^{p-q} \psi^R_{m,n}(r,0,z)\big|_{r=R^*,z=0} = 0, \tag{A2}$$

$$\partial_r^q \partial_r^{p-q} \psi^\varphi_{m,n}(r,0z)\big|_{r=R^*,z=0} = 0, \tag{A3}$$

where $p = 0,1,...,n-1$ and $q = 0,1,...,p$, was solved numerically, again using *Matlab*, for the variables $\{kR^*, a_2, a_3, ..., a_{\frac{1}{2}n(n+1)}, b_1, b_2, ..., b_{\frac{1}{2}n(n+1)}\}$. The resulting beam coefficients are listed in Table II.

Appendix B: Relationship between barrier intensity and trap separation

We consider an incoherent superposition of (scalar) fields $\Psi_{m,n}$ and $\Psi_{-m,n}$, and study the effect of the amplitude of the perturbation, ε, on the separation between neighbouring traps whose positions differ only in the

$(\lvert m\rvert, \lvert n\rvert)$	(5, 2)	(3,2)	(5,3)
kR^*	15.9999	15.0384	92.9998
a_1	1	1	1
a_2	1.77676	1.31264	-0.832378
a_3	2.90776	2.44492	0.527333
a_4			-0.234388
a_5			3.507096
a_6			-3.60292
b_1	0.981266	0.865462	0.953308
b_2	0.548220	0.424257	0.199681
b_3	0.771167	0.649072	0.255829
b_4			0.723029
b_5			0.614987
b_6			0.818274

TABLE II: Beam coefficients for the vector beams $\vec{\Psi}_{\pm5,\pm2}$ (used in Figs 6 and 11). Additionally, the coefficients for the vector beams $\vec{\Psi}_{\pm3,\pm2}$ and $\vec{\Psi}_{\pm5,\pm3}$ have also been calculated (but not used in figures).

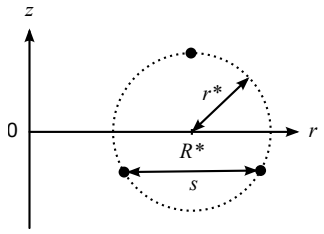

FIG. 12: Optical traps (black dots) whose positions differ only in their poloidal angle, shown in the radial plane in which they are located. The dotted circle is where the torus on which the vortex lines spiral intersects the plane, the z axis is the torus's axis of rotational symmetry, R^* and r^* are the major and minor radius of the torus, respectively, and s is the separation between neighbouring traps.

poloidal coordinate and on the minimum intensity separating neighbouring traps, the barrier intensity. By eliminating ε from the resulting equations we can then relate the barrier intensity to the trap separation.

We approximate the field $\psi_{m,n}$ (Eqn (1)) in a radial plane around the position where the charge-n vortex ring intersects the radial plane, i.e. around a point with coordinates $r = R^*$ and $z = 0$. We assume that the field there is of the form of a canonical vortex, namely

$$\psi_{m,n} = c_{m,n}\rho^n \exp(\mathrm{i}n\theta), \tag{B1}$$

where $c_{m,n}$ is a constant that depends on m and n, ρ is the distance from the vortex ring, and θ is the poloidal angle (Fig. 12). Note that this assumes the simplest case, as the field is in general not of the form of Eqn (B1) but instead stretched in the radial and longitudinal directions by different factors (which means that $K_- > 0$ in Eqn (2.2) in Ref. [11]).

The constant $c_{m,n}$ can be calculated by writing the magnitude of $\psi_{m,n}$ along a straight radial line through the charge-n vortex ring, i.e. a line given by the equations $\varphi = \varphi_0$ and $z = 0$, as a Taylor series around the radial coordinate of the charge-n vortex ring, $r = R^*$:

$$|\psi_{m,n}(r, \varphi_0, 0)| = \sum_{j=0}^{\infty} \frac{\partial_r^j F_{m,n}(r,0)\big|_{r=R^*}}{j!}(r - R^*)^j. \tag{B2}$$

From Eqn (A1) it is clear that the first $n-1$ terms in this sum are all zero, which means that the leading power is the nth power in $r - R^* = \rho$. The constant $c_{m,n}$ is simply the coefficient of this leading power.

$$c_{m,n} = \frac{\partial_r^n F_{m,n}(r,0)\big|_{r=R^*}}{n!}. \tag{B3}$$

This expression can be evaluated further using the standard properties of Bessel functions.

As in Eqn (4), we create the field $\Psi_{m,n}$ from the field $\psi_{m,n}$ by adding a perturbation in the form of a uniform plane wave, that is,

$$\varepsilon\psi_p = \varepsilon \exp(\mathrm{i}kz). \tag{B4}$$

In the radial plane $\varphi = \varphi_0$, the added perturbation splits the charge-n vortex in $\psi_{m,n}$ into n charge-1 vortices. These lie at positions where the magnitude of the unperturbed field equals that of the perturbation, and where the phases of these two fields are out by π. The charge-1 vortices therefore lie equally spaced on a circle centred at the position $r = R^*$ and $z = 0$ and of radius

$$r^* = \left|\frac{\varepsilon}{c_{m,n}}\right|^{1/n}. \tag{B5}$$

Of course, r^* is the minor radius of the torus on which the vortex lines spiral, and R^* is the major radius. Note that, in this analysis, the torus is undistorted due to our assumption that the original charge-n vortex line is canonical, Eqn (B1).

Now it is easy to calculate the separation s between neighbouring vortices, which becomes the separation between neighbouring traps if $\Psi_{-m,n}$ is incoherently added to $\Psi_{m,n}$. From Fig. 12, it can be seen that

$$s = 2r^* \sin\frac{\pi}{n} = 2\left|\frac{\varepsilon}{c_{m,n}}\right|^{1/n} \sin\frac{\pi}{n}. \tag{B6}$$

It is easy to see that, at least for small values of ε, the barrier intensity I_b separating neighbouring traps is given by the intensity at the position of the original charge-n vortex ring, which is simply given by the sum of the intensities of the fields $\Psi_{m,n}$ and $\Psi_{-m,n}$ there, each of which is simply the intensity (see Eqn (3)) of the perturbation:

$$I_b = 2A|\varepsilon|^2. \tag{B7}$$

Eliminating $|\varepsilon|$ from Eqns (B6) and (B7) gives

$$I_b = 2A\left|c_{m,n}\left(\frac{s}{2\sin(\pi/n)}\right)^n\right|^2. \tag{B8}$$

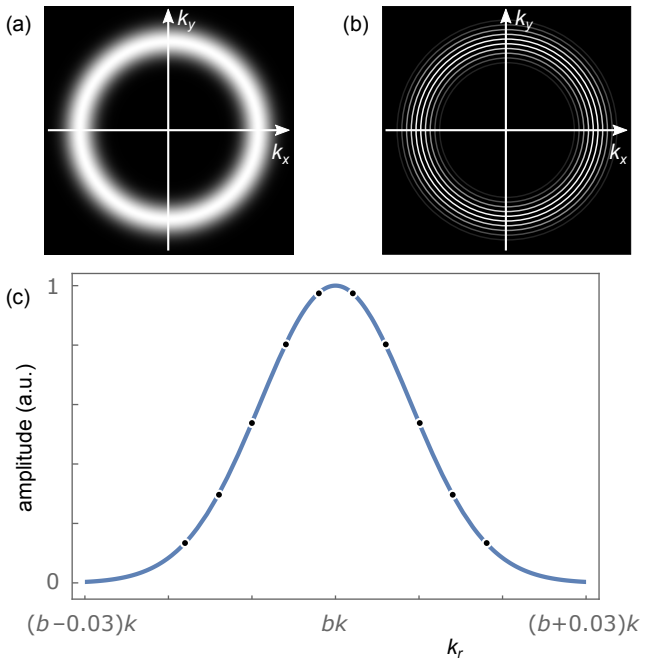

FIG. 13: Fourier-space structure of Bessel-Gauss beams and their approximation as a sum of Bessel beams. The plots in (a,b) show grayscale representations (black = 0, white = 1) of the amplitude distribution as a function of the transverse wave numbers, k_x and k_y, for a Bessel-Gauss beam (a) and for a superposition of 10 Bessel beams used to approximate this Bessel-Gauss beam. (c) Radial cross-sections through these distributions. The amplitude of the Bessel-Gauss beam is shown as a solid line, the amplitudes of the Bessel beams are indicated by black discs. Both are plotted as a function of $k_r = \sqrt{k_x^2 + k_y^2}$.

Specifically, it can be seen that the barrier intensity scales with the $(2n)$th power of the trap separation s:

$$I_b \propto s^{2n}. \tag{B9}$$

Appendix C: Simulation of vector Bessel-Gauss beams

As Bessel beams are mathematical idealisations and cannot be realised experimentally, they are usually replaced in experiments with Bessel-Gauss beams. In Fourier space, specifically when projected into the (k_x, k_y) plane, the infinitely thin ring of radius kb of an ideal Bessel beam then becomes blurred by a Gaussian function, resulting in an annulus with a Gaussian profile in the radial direction (Fig. 13(a)). This amplitude distribution can be approximated by a set of infinitely thin Bessel-beam rings of different radii, chosen such that the rings are equally spaced across the annulus, and amplitudes, chosen such that the amplitude of each ring is that of the Bessel-Gauss annulus at the same radius (Fig. 13(b)).

Similarly, a sum of N vector Bessel beams with suitable amplitudes and values b_i can be used to approximate a vector Bessel beam with given parameters m and b (Eqn (13)). Specifically, we choose the value of the b parameter of the ith ring to be $b_i = b + \Delta b_i$, where the Δb_is take the values ± 0.002, ± 0.006, ± 0.01, ± 0.014, and ± 0.018, and we set the amplitude of the ith ring to $\exp(-\Delta b_i^2/0.00016)$ (Fig. 13(c)), multiplied by the amplitude of the original vector Bessel beam.

Replacing Bessel-Gauss beams with a series of Bessel beams leads to artefacts in the form of periodicity in the radial direction. In our case, the period is $\approx 100R^*$. We avoid problems due to this periodicity by restricting ourselves to analysing the beam only within the region of the first period, namely for radii $r < 50R^*$.

Appendix D: Size-scalability of Bessel-beam superpositions

Our knot fields are superpositions of Bessel beams. Here we briefly discuss the size-scalability of Bessel-beam superpositions.

It is possible to scale a Bessel-beam superposition isotropically, but this involves changing the wavelength by the same scale factor, i.e. in the case of our knot fields by scaling k in Eqn (2) by the inverse of the scale factor.

For constant wavelength, scaling a Bessel-beam superposition in the transverse directions by a factor s can be achieved by transverse scaling of each of the Bessel beams in the superposition individually. In the case of the knot fields, scaling of the individual Bessel beams in Eqn (2) by s in the transverse direction is equivalent to dividing b_l by s. This, in turn, alters the longitudinal wave number $k\sqrt{1-b_l^2}$, thereby scaling all Bessel beams in the superposition in the longitudinal direction. Leaving out the plane-wave-like phase change on propagation leaves the "reduced" longitudinal wave number $k(\sqrt{1-b_l^2}-1)$.

In the paraxial limit, $b_l \ll 1$, dividing b_l by a factor s divides the "reduced" longitudinal wave numbers by s^2 independent of l, which corresponds to longitudinal stretching of the entire beam by a factor s^2. Note that, in all non-trivial cases, the longitudinal scaling factor is different from the transverse scaling factor, and so the aspect ratio of the superposition changes.

But non-paraxially, each Bessel beam in the superposition is scaled in the longitudinal direction by a different factor. This means that the superposition does not simply get stretched in the longitudinal direction, but it changes shape. This becomes particularly clear when the size is decreased in the transverse direction by so much that one or more of the b_l coefficients become greater than 1, which means that the corresponding Bessel beams become evanescent, i.e. change *amplitude* on propagation instead of phase. Note that in our simulations b_1 is chosen to be close to, or even equal to, 1 (see Tables I and II), and so the first Bessel component is close to, or even on, the borderline between travelling and evanescent.

[1] C. Cohen-Tannoudji and D. Guery-Odelin, *Advances in Atomic Physics: An Overview* (World Scientific, 2011).

[2] D. Schrader, S. Kuhr, W. Alt, M. Müller, V. Gomer, and D. Meschede, Appl. Phys. B **73**, 819 (2001).

[3] B. J. Bloom, T. L. Nicholson, J. R. Williams, S. L. Campbell, M. Bishof, X. Zhang, W. Zhang, S. L. Bromley, and J. Ye, Nature **506**, 71 (2014).

[4] M. Lewenstein, A. Sanpera, and V. Ahufinger, *Ultracold Atoms in Optical Lattices: Simulating Quantum Many Body Systems* (Oxford, 2012).

[5] D. Jaksch, C. Bruder, J. I. Cirac, C. W. Gardiner, and P. Zoller, Phys. Rev. Lett. **81**, 3108 (1998).

[6] J. Dalibard, F. Gerbier, G. Juzeliūnas, and P. Öhberg, Rev. Mod. Phys. **83**, 1523 (2011).

[7] T. Chakraborty and P. Pietilainen, *The Fractional Quantum Hall Effect* (Springer, 1988).

[8] R. B. Laughlin, Phys. Rev. Lett. **50**, 1395 (1983).

[9] F. D. M. Haldane, Phys. Rev. Lett. **55**, 2095 (1985).

[10] M. Łącki, M. A. Baranov, H. Pichler, and P. Zoller, Phys. Rev. Lett. **117**, 233001 (2016).

[11] M. V. Berry and M. R. Dennis, Proc. R. Soc. Lond. A **457**, 2251 (2001).

[12] J. Leach, M. Dennis, J. Courtial, and M. Padgett, Nature **432**, 165 (2004).

[13] J. Leach, M. R. Dennis, J. Courtial, and M. J. Padgett, New J. Phys. **7**, 55 (2005).

[14] M. R. Dennis, R. P. King, B. Jack, K. O'Holleran, and M. J. Padgett, Nature Physics **6**, 118 (2010).

[15] I. Freund, Opt. Commun. **159**, 99 (1999).

[16] Z. Bouchal and M. Olivík, J. Mod. Opt. **42**, 1555 (1995).

[17] H. J. Metcalf and P. van der Straten, "Laser cooling and trapping," (Springer-Verlag, New York, 1999) p. 274.

[18] M. Egorov, B. Opanchuk, P. Drummond, B. V. Hall, P. Hannaford, and A. I. Sidorov, Phys. Rev. A **87**, 053614 (2013).

[19] R. Grimm, M. Weidemüller, and Y. B. Ovchinnikov, Adv. Opt. Photon. **42**, 95 (2000).

[20] M. H. Anderson, J. R. Ensher, M. R. Matthews, C. E. Wieman, and E. A. Cornell, Science **269**, 198 (1995).

[21] F. Gori, G. Guattari, and C. Padovani, Optics Communications **64**, 491 (1987).

[22] M. Berry, in *Fundamental Problems in Quantum Theory*, edited by J. A. Anandan and J. Safko (World Scientific, Singapore, 1994).

[23] M. R. Dennis, A. C. Hamilton, and J. Courtial, Opt. Lett. **33**, 2976 (2008).

[24] S. Zhang, F. Robicheaux, and M. Saffman, Phys. Rev. A **84**, 043408 (2011).

[25] C. C. Adams, *The Knot Book* (W.H. Freeman and Co., New York, 1994).

[26] C. Livingston, *Knot Theory* (Cambridge University Press, 1993).

[27] If m and n are coprime, the vortex lines form an $(m;n)$ torus knot [25], which winds n times around a circle in the interior of the torus (in the poloidal direction), and m times around its axis of rotational symmetry (i.e. in the toroidal direction) [26]; if m and n have a common factor, N, the vortex lines form N linked rings or torus knots.

[28] It will be possible to image the volume around the ring with a transverse magnification close to 1 without destroying the trap configuration. We have not investigated *how* close to 1 the transverse magnification has to be before the trap configuration breaks down.